Published in final edited form as:

Biochemistry. 2016 May 10; 55(18): 2622–2631. doi:10.1021/acs.biochem.6b00239.

Replacing Arginine 33 for Alanine in the Hemophore HasA from *Pseudomonas aeruginosa* Causes Closure of the H32 Loop in the Apo-Protein

Ritesh Kumar[¥,‡], **Yifei Qi**[¥], **Hirotoshi Matsumura**[€,‖], **Scott Lovell**[¢], **Huili Yao**[£], **Kevin P. Battaile**[¶], **Wonpil Im**[¥], **Pierre Moënne-Loccoz**[€], and **Mario Rivera**[£,*]

[£]Department of Chemistry, University of Kansas, Multidisciplinary Research Building, 2030 Becker Dr. Lawrence, KS 66047, United States

[¥]Center for Computational Biology and Department of Molecular Biosciences, Multidisciplinary Research Building, University of Kansas, 2030 Becker Dr., Lawrence, KS 66047, United States

[¢]Protein Structure Lab, Del Shankel Structural Biology Center, University of Kansas, 2034 Becker Drive, Lawrence, Kansas 66047, United States

[€]Division of Environmental & Biomolecular Systems, Institute of Environmental Health, Oregon Health and Science University, 3181 SW Sam Jackson Park Road, Oregon 97239, United States

[¶]IMCA-CAT, Hauptman Woodward Medical Research Institute, 9700 South Cass Avenue, Bldg. 435A, Argonne, Illinois 60439, United States

Abstract

Previous characterization of hemophores from *Serratia marcescens* (HasAs), *Pseudomonas aeruginosa* (HasAp) and *Yersinia pestis* ($HasA_{yp}$) showed that hemin binds between two loops, where it is axially coordinated by H32 and Y75. The Y75 loop is structurally conserved in all three hemophores and harbors conserved ligand Y75. The other loop contains H32 in HasAs and HasAp, but a noncoordinating Q32 in $HasA_{yp}$. The H32 loop in apo-HasAs and apo-HasAp is in an open conformation, which places H32 about 30 Å from the hemin-binding site. Hence, hemin binding onto the Y75 loop of HasAs or HasAp triggers a large relocation of the H32 loop from an open- to a closed-loop conformation and enables coordination of the hemin-iron by H32. In comparison, the Q32 loop in apo-$HasA_{yp}$ is in the closed conformation and hemin binding occurs with minimal reorganization and without coordinative interactions with the Q32 loop. Studies in crystallo and in solution have established that the open H32 loop in apo-HasAp and apo-HasAs is well structured and minimally affected by conformational dynamics. In this study we address the intriguing issue of the stability of the H32 loop in apo-HasAp and how hemin binding triggers its relocation. We address this question with a combination of NMR spectroscopy, X-ray

[*]Corresponding author: Mario Rivera, Department of Chemistry, University of Kansas, Multidisciplinary Research Building, 2030 Becker Dr., Lawrence, KS 66047. Telephone: 503-864-4936; Fax: 785-864-1916; mrivera@ku.edu.

[‡]Present address: 1Globe Health Institute, 333 Providence Highway, Norwood 02062 Massachusetts

[‖]Present address: Department of Life Science, Faculty and Graduate School of Engineering and Resource Science, Akita University, 1-1 Tegata Gakuen-machi, Akita City, Akita, 010-8502 Japan

[ξ]Coordinates and crystallographic structure factors for the R33A apo- and holo HasAp structures have been deposited in the protein data bank under accession codes 5IQW (R33A apo-HasAp) and 5IQX (R33A holo-HasAp)

crystallography, and molecular dynamics simulations and find that R33 is critical to the stability of the open H32 loop. Replacing R33 with A causes the H32 loop in R33A apo-HasAp to adopt a conformation similar to that of holo-HasAp. Finally, stopped-flow absorption and resonance Raman analyses of hemin binding to apo-R33A HasAp indicates that the closed H32 loop slows down the insertion of the heme inside the binding pocket, presumably as it obstructs access to the hydrophobic platform on the Y75 loop, but accelerate the completion of the heme iron coordination.

INTRODUCTION

Iron and iron-binding proteins are required for physiologically important functions like DNA biosynthesis, gene regulation, respiration, and degradation of xenobiotics.[1,2] In biological fluids the concentration of free iron is maintained at extremely low levels (~10^{-18} M) by sequestration of the micronutrient in iron-binding proteins such as transferrin and lactoferrin.[3] The low concentration of free iron in vertebrate hosts poses a challenge for pathogenic bacteria, which have evolved several mechanisms to circumvent the nutritional immunity imposed by mammalian hosts.[4–6] Several pathogens utilize heme as an iron source, including the opportunistic *P. aeruginosa*, which encodes two heme uptake systems, the *Pseudomonas* heme uptake (*phu*) and the heme assimilation (*has*) systems.[4,7,8] The *phu* operon encodes the receptor PhuR, which binds heme and transports it to the periplasm, whereas the *has* operon encodes a secreted hemophore (HasA) to capture heme and deliver it to the HasR receptor for subsequent internalization.[4,8,9] Recent studies suggest that in the airways of cystic fibrosis patients, *P. aeruginosa* can acquire mutations in the promoter of the *phu* operon that increase its expression, endowing these strains with a growth advantage in the presence of hemoglobin.[10] Along this vein, Smith and Wilks studied the differential contributions of PhuR and HasR to heme acquisition in *P. aeruginosa* and proposed a model where PhuR and HasR are non-redundant heme receptors.[11] In this model, the HasA-HasR system functions primarily as a sensor of extracellular heme, whereby heme binding to HasA stimulates heme uptake via PhuR. The high avidity of HasA for heme allows sensing and capturing heme at very low concentrations.

Structural and biochemical studies of hemophore proteins from Gram-negatives such as *Serratia marcescens* (HasAs),[12,13] *Pseudomonas aeruginosa* (HasAp)[14,15] and *Yersinia pestis* ($HasA_{yp}$)[16] have been reported. The X-ray crystal structures of heme-bound (holo) hemophores HasAs[12] and HasAp[15] revealed a unique fold (Figure 1A), where one side of the protein is made of α-helices and the other is composed of antiparallel β-sheets; the two sides are connected by two long loops. One of the loops harbors the proximal heme ligand (Y75) and is therefore termed the Y75 loop, whereas the second loop contains the distal heme ligand (H32) and is called the H32 loop. Structural characterization of the heme-free, apo-HasAs in solution by NMR spectroscopy[13] and of apo-HasAp by X-ray crystallography[14] shows a fold similar to that of the holo-hemophore, except for the H32 loop, which is in an open conformation and folded back over the body of the protein (Figure 1B). Hence, upon heme loading the H32 loop undergoes a large conformational rearrangement which relocates the H32 ligand ~30 Å from the open to a closed state, thus enabling coordination of the heme-iron by His32 from the distal site.[13,14,17] Amino acid

sequence analysis indicates that Tyr75 is conserved among the HasA sequences but that there is no conservation of His32.[14,16] Hemophore sequences from the *Yersinia* species contain a Gln residue at the position equivalent to His32 in HasAs and HasAp. In the case of $HasA_{yp}$, structural studies carried out with apo- and holo-$HasA_{yp}$[16] indicate that the Y75 loop structure is identical to HasAp and HasAs in the apo- and holo-proteins. In contrast, the Q32-bearing loop in apo-$HasA_{yp}$ is in the closed conformation and undergoes only minimum structural changes upon heme binding.[16]

The closed conformation of the H32 loop in holo-HasAp is stabilized by the coordination bond between H32 and the hemin iron, and by a network of interactions involving D29, R33, Y138 and S142 (Figure 1D). Despite the large rearrangement undergone by the H32 loop in HasAp and HasAs upon heme binding, NMR spectroscopy and X-ray crystallography indicate that the loop in the apo hemophores does not experience conformational disorder.[13,14,16] The stability of the H32 loop in the apo-proteins is probably a consequence of a “zipper-like” network of interactions with the outer surface of the protein core domain, which stabilize the open conformation and prevent dynamic conformational disorder. A detailed comparative analysis of interactions along the H32 loop in apo-HasAp suggested that Arg33 plays a pivotal role in anchoring the H32 loop via a network of salt bridge and H-bond interactions with Glu113 and Asp22 and hydrophobic and π-cation interactions with Y26 (Figure 1C). To test this idea, we replaced Arg33 for alanine (R33A) in HasAp. Results obtained from NMR spectroscopy in solution, and an X-ray crystal structure of the R33A apo-HasAp protein indicate that replacing Arg33 for alanine causes the H32 loop in the apo-protein to adopt a conformation very similar to that of holo-HasAp. Molecular dynamics (MD) simulations provide additional complementary insight into the H32 loop transition from open to closed conformations. Stopped-flow UV-vis and rapid-freeze-quench resonance Raman (RFQ-RR) spectroscopies show that the R33A variant reaches an identical holo structure as the wild type (WT) protein but through different kinetics, as the initial capture of hemin is hampered by the non-native, closed conformation of the H32 loop.

EXPERIMENTAL PROCEDURES

Site-directed mutagenesis

The pET11a vector harboring a truncated gene of HasAp missing the last 21 C-terminal residues[15] was used to construct the R33A mutant. The primers, synthesized by Integrated DNA Technologies, Inc. (Coralville, IA), were used with the QuickChange site-directed mutagenesis kit (Stratagene; La Jolla, CA). Primers used to introduce the R33A mutation were 5′-TATTTTGGCGATGTGAACCATGCGCCGGGCCAGGT-GGTGGATGGC-3′ and 5′-GCCATCCACCACCTGGCCCGGCGCATGGTTCACATCGCC-AAAATA-3′, where the underlined codons represent target substitutions. The recombinant gene harboring the mutation was transformed into XL1-Blue Competent cells (Stratagene) for amplification, and the DNA sequence verified by ACGT Inc. (Wheeling, IL). The recombinant DNA plasmid with the correct sequence was transformed into *E. coli* BL21-GOLD (DE3) competent cells (Agilent Technologies, CA) for subsequent protein expression. The protocols for protein expression, purification of the apo-proteins and reconstitution with heme, have been described previously.[14]

Crystallization and Data Collection

All crystallization experiments were conducted in Compact 300 or CombiClover 500 (Rigaku Reagents) sitting drop vapor diffusion plates. Equal volumes (0.5 μL) of each, protein and crystallization solution were mixed and equilibrated against 100 μL of the reservoir solutions. Crystals were cryo-protected by transferring to a solution containing 80% crystallization solution and 20% glycerol before freezing in liquid nitrogen.

R33A apo-HasAp—A protein sample (50 mg/mL) in 100 mM sodium phosphate buffer pH 7.8 yielded prism shaped crystals in about 40 days from the Crystal Screen (Hampton Research) condition G10 (0.05 M Cd(SO_4) hydrate, 0.1 M HEPES pH 7.5, 1.0 M sodium acetate trihydrate).

R33A holo-HasAp—Protein (20 mg/mL) in 100 mM sodium phosphate buffer pH 7.8 produced plate shaped crystals within 72 h from the Wizard III & IV (Rigaku Reagents) condition G8 (2100 mM DL-malic acid, pH 7.0).

Initial X-ray diffraction data were collected in-house using a Rigaku RU-H3R rotating anode generator equipped with Osmic Blue focusing mirror and an R-axis IV^{++} image plate detector. High-resolution diffraction data were acquired at 100 K at the Advanced Photon Source (APS) IMCA-CAT beamline 17ID using a Dectris Pilatus 6M pixel array detector.

Structure Solution and Refinement

Diffraction intensities were integrated and scaled using the XDS[18] and scaling/Laue class analyses were carried out with Aimless.[19 20] Structure solutions for apo- and holo-proteins were obtained by molecular replacement with Phaser[21] via the Phenix[22] interface, using the coordinates from the structure of WT holo-HasAp (PDB code: 3ELL). Structure refinement and manual model building for apo- and holo-proteins were performed with Phenix[22] and Coot[23] respectively. Structure validation was carried out using Molprobity[24] and figures were prepared using CCP4mg[25] and PyMol.[26] X-ray data collection and refinement statistics are summarized in Table 1.

R33A apo-HasAp—Initial structure solution and refinement were done using in-house diffraction data collected with Cu-K_α radiation. Crystals were indexed in a primitive tetragonal Bravais lattice with a Laue class of 4/*mmm* and possible space groups $P4_12_12$ or $P4_32_12$. All space groups with 422 point symmetry were searched during molecular replacement. The top solution was obtained in $P4_12_12$. The Matthews coefficient[27,28] analysis via CCP4[25] suggested that there were two molecules in the asymmetric unit. However, the top molecular replacement solution consisted of a single molecule in the asymmetric unit with ~ 70% solvent content. During the refinement, large anomalous difference electron density peaks (F_o - F_c) greater than 20σ were observed that were tentatively assigned as cadmium ions from the crystallization solution. Consequently, synchrotron data were collected at two different wavelengths to analyze the anomalous signal. The data set collected at λ = 1.7396 Å (7,150.1 eV) yielded strong anomalous electron density and the set collected at λ = 1.0000 Å (12,394 eV) yielded an appreciable yet smaller anomalous signal. The DelAnom correlation between half-sets, a metric of

anomalous signal strength, determined during scaling with Aimless were 0.43 and 0.83 for the high and low energy wavelengths, respectively. Using the two data sets, anomalous Fourier difference electron density maps were calculated for the three cadmium ions that were assigned (Figure S1). Table S1 lists the peak height of each of the three cadmium ions from the anomalous Fourier difference electron density maps. Notably, the anomalous signal increases at the longer wavelength supporting the assignment of cadmium ions at these sites. Additionally, a large region of electron density was observed near G44, positioned between strands β2, β3 and β6, as shown in Figure S2. This electron density was left unassigned as it did not correspond to compounds that were in contact with the protein from expression to cryoprotection of the crystals.

R33A holo-HasAp—Crystals of holo-HasAp R33A were indexed as primitive orthorhombic lattice (*mmm*). Molecular replacement searches using Phenix were conducted in all space groups with 222 point symmetry, and the top solution was obtained in $P2_12_12_1$ with one molecule in the asymmetric unit. Refinement was conducted with anisotropic atomic displacement parameter for all atoms. Three sodium ions and a disordered malate molecule were modeled in the final structure. Table 1 summarizes the crystallographic details for the structures.

NMR Spectroscopy

Uniformly labeled U-^{15}N-R33A HasAp were prepared with minor modification of the above-described protocol: Overnight culture was resuspended in M9 media with 1.0 g of $^{15}NH_4Cl$. IPTG (final concentration of 1 mM) was added when the culture reached OD_{600} ~ 0.9; cells were harvested and the protein was purified as described above. ^{15}N-^{1}H-HSQC spectra were obtained on a Bruker Avance spectrometer operating at a frequency of 599.740 MHz (^{1}H frequency) using the following parameters: 2048 (^{1}H) × 256 (^{15}N) complex points; 10.7 kHz (^{1}H) and 2.4 kHz (^{15}N) spectral widths; 32 scans per increment; relaxation delay d1 = 1s.

Molecular Dynamics Simulations

The initial simulation systems were generated with the Quick MD Simulator module in CHARMM-GUI.[29,30,31] The protein was solvated in an 81×81×81 Å^3 TIP3P water box and buffered with 0.15 M NaCl. For both wild type and R33A mutant prepared by CHARMM-GUI PDB Manipulator[32], three independent MD simulations with different initial velocities were performed using the CHARMM force field[33,34] in NPT (constant particle number, pressure, and temperature) ensemble with the temperature maintained at 300 K using Langevin dynamics and pressure maintained at 1 bar with the Nose-Hoover piston method.[35,36] The van der Waals interactions were switched off at 10–12 Å by a force switching function,[37] and the electrostatic interactions were calculated using the particle-mesh Ewald method.[38] The time step was 2 fs, and each system was simulated for 100 ns using NAMD.[34]

RR and EPR Spectroscopy

RR spectra were obtained using a McPherson 2061/207 spectrograph (0.67 m with variable gratings) equipped with a Princeton Instruments liquid N_2-cooled CCD detector

(LN-1100PB). The 407-nm line of a krypton laser (Innova 302, Coherent) was used as the Raman excitation source. A long-pass filter (RazorEdge, Semrock) was used to attenuate Rayleigh scattering. Spectra at room temperature were collected in a 90° scattering geometry on samples mounted on a reciprocating translation stage. Frequencies were calibrated relative to indene and CCl_4 and are accurate to ±1 cm^{-1}. CCl_4 was also used to check the polarization conditions. Low temperature spectra were obtained in a backscattering geometry on samples maintained at ~ 110 K in a liquid nitrogen cold finger. Frequencies were calibrated relative to aspirin and are accurate to ±1 cm^{-1}. The integrity of the RR samples, before and after laser illumination, was confirmed by direct monitoring of their UV-Vis spectra in the Raman capillaries. EPR spectra were recorded on a Bruker E500 X-band EPR spectrometer equipped with a superX microwave bridge, a dual mode cavity and a helium-flow cryostat (ESR 900, Oxford Instruments, Inc.).

Stopped-flow UV-vis spectroscopy

Stopped-flow experiments were performed with an SX20 stopped-flow UV-vis spectrometer (Applied Photophysics) with a 1-cm path length cell equilibrated at 4 °C. Apo-HasAp protein solutions were prepared at concentrations ranging from ~ 40 to 400 μM in 200 mM HEPES buffer, pH 7.0, using a 280-nm molar extinction coefficient, ε_{280}, of 27 $mM^{-1}cm^{-1}$. Hemin was dissolved in 10 mM NaOH and diluted to a final concentration of 10 μM just before the stopped-flow experiments using an ε_{385} of 58.4 $mM^{-1}cm^{-1}$. After each measurement, remaining pre-mixed solutions were recovered from the stopped-flow apparatus to confirm the protein and hemin concentrations. The time-resolved spectra were examined by global analysis using a Marquardt-Levenberg algorithm (Pro-K software, Applied Photophysics). Reported rate constants are the average of at least three different rapid mixing experiments.

Rapid freeze quench experiments

Details of our protocols for the preparation of RFQ samples were published recently.[39] Briefly, glass syringes (2 mL) loaded with 0.6 mM apo-HasAp proteins in 200 mM HEPES, pH 7.0 and 0.6 mM hemin solution in 10 mM NaOH were mounted to a System 1000 Chemical/Freeze Quench Apparatus (Update Instruments) and maintained at 4 °C with a water bath. Reaction times were controlled by varying the syringe displacement rate from 2 to 8 cm/s or by varying the length of the reactor hose after the mixer. Mixed samples of 250 μL were trapped in liquid ethane at or below −120 °C in glass funnels attached to NMR tubes. Liquid ethane was subsequently removed by incubating samples at −80 °C for 2 hours. RR spectra obtained before and after removal of ethane showed no spectral changes except for the loss of ethane bands.

RESULTS AND DISCUSSION

R33A apo- and holo-HasAp are purified to homogeneity as monomeric proteins

A previously reported chromatographic protocol[14] was used to purify R33A apo-HasAp. The corresponding holo-protein was prepared from the apo-protein by reconstitution with heme *in vitro*, as described previously.[14] Protein homogeneity was checked using SDS PAGE, which showed a single band corresponding to a molecular mass of ~19 kDa. The

experimental molecular mass determined by electrospray ionization mass spectrometry is 18,673 Da., which is in good agreement with the molecular mass calculated from the amino acid sequence, 18,674 Da, without the initiator methionine.

The spectroscopic characterization of R33A holo-HasAp matches that of WT holo-HasAp

The UV-vis absorption spectrum of R33A holo-HasAp is identical to that of WT holo-HasAp with a Soret peak at 407 nm (ε_{407} = 144.2 mM^{-1} cm^{-1}) and visible absorption bands at 495, 540, 577, and 617 nm (Figure S3). The absorption maximum of the Soret peak and the charge transfer band at 617 nm are indicative of a high-spin ferric heme, whereas the Q bands at 540 and 577 nm are indicative of a low-spin species. Room-temperature resonance Raman (RR) spectra of R33A holo-HasAp further support the conservation of the six-coordinate high-spin/six-coordinate low-spin (6cHS/6cLS) equilibrium mixture previously observed with WT holo-HasAp.[15] Specifically, ν_3 modes at 1477 and 1505 cm^{-1}, ν_2 at 1561 and 1579 cm^{-1}, and ν_{10} at 1606 and 1635 cm^{-1} for high-spin and low-spin conformers, respectively, are observed with very similar intensities in the high-frequency RR spectra of R33A and WT holo-HasAp (Figure S4). RR spectra obtained at cryogenic temperatures are dominated by contributions for the low-spin conformers, and once again are very similar for R33A and WT holo-proteins (Figure S4). The EPR spectrum of R33A holo-HasAp is also virtually identical to that of WT holo-HasAp with a dominant $S = 1/2$ rhombic signal with g = 2.84, 2.21, and 1.72 (Figure S5).

NMR spectroscopic characterization of R33A apo- and holo-HasAp in solution suggests that the H32 loop in the apo-protein is no longer in the open conformation

The ^{1}H, ^{15}N-HSQC spectrum of R33A apo-HasAp is significantly different from that of the wt-apo protein (Figure 2A), indicating significant structural differences between the mutant and WT apo-proteins. As mentioned above, the side chain of Arg33 appears to play a central role in mediating a network of interactions that restrain the H32 loop against the protein structure. Hence, the large changes in the HSQC spectrum of R33A apo-HasAp suggest that the H32 loop may no longer be organized as in the WT apo-protein. In addition, HSQC spectra of the R33A apo-protein taken at 15 °C and 25 °C do not show significant perturbations in the chemical shifts or shape of the cross peaks, suggesting that all observable cross peaks in R33A apo-HasAp originate from well-structured portions of the protein. When the R33A apo-protein is reconstituted with hemin, the HSQC spectrum of the resultant holo-protein is nearly identical to that of the WT holo-protein (Figure 2B). This observation indicates that upon heme binding the H32 loop in the R33A protein adopts a conformation nearly identical to that observed in the WT holo-protein. Together, the above observations suggest that in the R33A apo-protein the H32 loop is no longer organized as in the WT apo-protein. Binding of heme, however, causes the H32 loop in the mutant to adopt a conformation nearly identical to that observed in WT holo-HasAp. To provide additional evidence for this these structural rearrangements we determined the crystal structure of R33A HasAp in its apo- and heme-bound forms.

The H32 loop in Arg33 apo-HasAp adopts a closed conformation

The X-ray crystal structure of R33A apo-HasAp was refined to a resolution of 1.94 Å (Table 1). Electron density was traced from Ser2 to Ala184, except for five residues (Gly35 to

Asp39) located in the His32 loop, for which electron density was not observed (Figure 3A). The overall fold is nearly unchanged relative to that of the WT apo-protein, except for the His32 loop (shown in magenta), which adopts a significantly different conformation, as can be seen in the superposition of the WT and R33A apo-protein structures (Figure 3B). The structural superposition of R33A apo-HasAp with WT holo-HasAp (Figure 3C) shows that although the loop in the R33A mutant is not completely defined, the segments defined by electron density adopt a conformation similar to that seen for the H32 loop in WT holo-HasAp (orange). In a previous study we determined the structures of the *Yersinia pestis* $HasA_{yp}$ in its apo- and holo-forms,[16] which harbors a Gln, rather than His at position 32. We observed that in contrast to apo-HasAs and apo-HasAp, the loop in apo-$HasA_{yp}$ is already in the closed conformation. Moreover, hemin binding to apo-$HasA_{yp}$ does not cause significant perturbations in the structure and no residue from the Q32 loop in holo-$HasA_{yp}$ binds the hemin-iron. Superposing the structure of R33 apo-HasAp with the structures of apo- and holo-$HasA_{yp}$ shows that the conformation of the H32 loop in R33 apo-HasAp is very similar to that adopted by the Q32 loop in apo- and holo-$HasA_{yp}$ (Figure 3-D).

In WT apo-HasAp a network of backbone and side-chain hydrogen bonding interactions stabilize the open conformation of the H32 loop (Figure 1C and Table 2). The conformation of the H32 loop in WT apo-HasAp is not affected by disorder or by dynamic conformational disorder. Clear evidence for this stems from (*i*) the X-ray crystal structure of apo-HasAp, where the H32 loop is defined by clear electron density and by *B*-factors similar to the average *B*-factor for the structure,[14,15] and (*ii*) NMR spectroscopy in solution, showing that in ^{1}H, ^{15}N-HSQC NMR spectra, cross-peaks originating from the loop residues do not indicate conformational dynamics.[40] It is therefore interesting that despite the network of interactions stabilizing the loop against the body of the protein, replacement of a single residue, Arg33, causes the loop to detach from the body of the protein, move toward the Y75 loop, and adopt a conformation similar to that observed for the closed conformation in holo-HasAp. The pivotal role played by R33 is probably a consequence of key salt bridge and hydrogen bonding interactions (Figure 1-C) between the guanidinium group of R33 (N_{H1}, N_{H2}, N_{ε}), the carboxylate groups of E113 ($O_{\varepsilon 1}$, $O_{\varepsilon 2}$) on strand $\beta 7$ and of D22 ($O_{\delta 2}$) from helix $\alpha 1$, and van der Waals contacts with the side chain of Y26. In the R33A mutant these stabilizing interactions are lost and the H32 loop adopts a conformation similar to that of the closed loop in holo-HasAp.

The structure of R33A holo-HasAp is identical to that of the WT holo-hemophore

The crystal structure of R33A holo-HasAp was refined to a resolution of 1.05 Å. The structure is nearly identical to that of the WT holo-protein (C_{α} root mean square deviation (RMSD) = 0.22 Å),[41] with the heme iron coordinated by H32 and Y75 (Figure 4-A). The Y75 loop in the mutant protein adopts a conformation virtually identical to that in the WT holo-protein. In the H32 loop, residues V38 to S41 adopt conformations distinct from those observed for the equivalent residues in the WT structure. Note that in the X-ray crystal structure of the R33A apo-protein these residues are disordered and therefore not modeled due to absence of electron density. Despite the small conformational changes in the H32 loop, the H32 imidazole N_{δ} still coordinates the heme-iron ion and the side chain adopts the same conformation as in the WT holo-protein. An interesting difference between the

structures of WT and R33A holo-HasAp is the orientation of the hemin molecule. In WT holo-protein, as well as in other mutants for which structures are available (Y75A, H83A), hemin binds to the hemophore in only one orientation.[14,15,40] In the R33A mutant hemin binds in two orientations which differ by a 180° rotation about the α-γ meso axis. Evidence for this mode of binding is manifest in the F_o-F_c electron density omit map (Figure 4B) contoured at 3σ. The best model was obtained with 50% occupancy of each of the heme orientations.

Molecular dynamics simulations support a closed configuration of the H32 Loop in R33A apo-HasAp

Additional insight into the position of the H32 loop in the R33A apo-HasAp molecule was obtained from MD simulations. MD trajectories were obtained for three different systems (R33A1, R33A2 and R33A3), as described in the Experimental Procedures (see movies S1 and S2 in Supporting Information). The start point of the MD trajectories for both, WT and R33A HasAp was the crystal structure of WT apo-HasAp, where the H32 loop (green in Figure 5B) is in the open conformation. Plots of the protein backbone RMSD from the WT apo-HasAp structure as a function of time (Figure 5A) show that the WT apo-protein remains nearly unchanged during the length of the simulation, with the H32 loop in the open conformation. Although these observations are in agreement with the aforementioned experimental findings made with X-ray crystallography and NMR spectroscopy, it is conceivable that conformational fluctuations might be observable if the MD simulations could be extended into the μs or longer time regime. In contrast, the MD trajectories obtained from the R33A mutant show relatively large RMSD, which are confined to residues in the H32 loop. The plots in Figure 5A also show that although the start of the structural changes (RMSD) is different for each of the three independent simulations, all systems converge at the end of the trajectories. As an example of the structural rearrangements that take place during the MD trajectories, Figure 5B shows the conformation of the H32 loop (blue) at the end of the MD trajectory obtained from system R33A1. It is evident that in the MD simulations the H32 loop adopts a closed conformation similar to that observed in the X-ray crystal structure of R33A apo-HasAp (magenta). Similarly, superposition of the R33A1 model obtained at the end of the trajectory (blue in Figure 6C) with the crystal structure of WT holo-HasAp (orange) provides additional support for a closed conformation of the H32 loop in the R33A apo-protein.

Hemin binding to R33A apo-HasAp proceeds slowly, within the millisecond timescale, but without build-up of a tyrosine-bound high-spin intermediate

Stopped-flow absorption experiments monitoring the binding of hemin to R33A apo-HasAp are shown in Figure 6. A rapid growth of Soret absorbance at 407 nm is clearly observed within the millisecond scale, but there is no evidence of Soret absorption features other than that of the starting hemin and of R33A holo-HasAp. This lack of a distinctive intermediate complex between hemin and R33A apo-HasAp is in sharp contrast with the stopped-flow data obtained with WT apo-HasAp, which showed an initial Soret absorption maximum at 403 nm accompanied by an intense high-spin marker band at 622 nm before formation of the holo protein with a Soret maximum at 408 nm.[17] Despite the lack of distinctive intermediate features, single wavelength analyses of the stopped-flow traces for R33A HasAp reveal a

biphasic behavior with a first observed rate, k_{obs1}, which increases with increasing apo-protein concentrations, but that remains quite slow compared to the initial phase observed in WT HasAp (Figure 6). As done previously with WT HasAp, we analyzed this hyperbolic dependence of k_{obs1} on apo-protein concentration with a two-step model where formation of a reversible hemin-apoprotein complex is followed by an iron coordination step (Scheme 1).

$$k_{obs1} = k_{1\,coord} \,^{*}[\text{apoprotein}]/((k_{-1}+k_{1\,coord})/k_1+[\text{apoprotein}]$$
$$\text{assuming } k_1 \,^{*}[apoprotein] \text{ and } k_{-1} \gg k_{1\,coord} \gg k_{-hemin}$$
$$k_{obs1} \approx k_{1\,coord} \,^{*}[\text{apoprotein}]/K_d+[\text{apoprotein}] \quad (1)$$

Using eq 1 to fit the dependence of k_{obs1} on the apo-protein concentration yields K_d and k_{1coord} and shows that the low k_{obs1} values measured with R33A apo-HasAp reflect a ~4-fold increase in K_d relative to WT apo-HasAp. Presumably, steric clashes between the H32 loop and the heme docking the hydrophobic surface composed by the Y75 loop are at the origin of this higher K_d value. Interestingly, k_{obs2} values in R33A are 3 to 4 times faster than in WT HasAp, where this later phase corresponds to the closing of loop H32 on the heme moiety. Overall, this kinetic scheme is very different than that of apo-$HasA_{yp}$ where the closed loop conformation is native to the WT protein and results in a barrierless formation of the holo-protein.[16]

The RFQ-RR characterization of the reaction of R33A apo-HasAp with hemin provides additional insight on the coordination steps that are taking place during the reaction. Specifically, the high-frequency RR spectrum of the 6-ms RFQ sample shows two components in the ν_3 region, at 1493 and 1506 cm^{-1}, characteristic of 5cHS and 6cLS heme species, respectively (Figure 7); most importantly, the intensity of these ν_3 modes are low relative to the dominant ν_4 and ν_2 modes at 1376 and 1580 cm^{-1}, respectively (Figure 7). As the aging time of the RFQ samples increases, the ν_3 band at 1493 cm^{-1} decreases in favor of the 1506 cm^{-1} band from the 6cLS species. The weak ν_3 mode at 1493 cm^{-1} in the 6-ms RFQ sample of R33A is in sharp contrast with the corresponding intensities in the RFQ-RR spectra of WT and H32A HasAp,[17] where the formation of transient 5cHS and 6cHS species with O-atom axial coordination leads to intense ν_3 modes at 1479 and 1489 cm^{-1}, respectively. Thus, these RFQ-RR data indicate that Tyr75 is not the first coordinating ligand to the heme iron(III) in the R33A variant. Since the crystal structure of R33A apo-HasAp shows the H32 loop hovering above the hemin binding pocket, it is tempting to propose that His32 is the first axial ligand to the heme iron before further axial coordination by Tyr35 to produce the 6cLS complex observed in R33A holo-HasAp.

Concluding remarks

Prior investigations provided experimental evidence for an induced-fit mechanism of hemin binding to the hemophore HasA.[13] Investigations carried out with HasAp have shown that hemin loads onto the Y75 loop and coordinates to Tyr75 on the millisecond scale at 4 °C. This rapid process is followed by significantly slower coordination of the heme by His32, which is complete in ~1 s.[14,17] Structural alignment of apo- and holo-HasAp shows that the majority of the structures are superimposable, including the structure of the Y75 loop. In contrast, the structure of the H32 loop undergoes large reorganization to its closed

conformation in holo-HasAp. In apo-HasAp, the Y75 loop is largely pre-organized and provides a hydrophobic “sticky” platform that can attract the porphyrin macrocycle through extensive hydrophobic and π−π stacking interactions; axial hemin ligation, which occurs after hemin capture, probably functions to slow hemin release and for delivering hemin to its cognate receptor.[14,16,40] Moreover, the phenolate side chain of Tyr75 is conformationally restricted by its hydrogen bond interaction with His83 N_{δ}, and axial coordination of the hemin-iron by Tyr75 can proceed rapidly with minimal structural reorganization of the Y75 loop.[40] However, sensing of hemin binding by the relatively remote H32 loop leads to loop closure and to the relatively slower coordination of the hemin iron by His32.[14,17] Closure of the H32 loop requires an extended interaction network between the heme binding site and the remote anchoring of the H32 loop in its open conformation.[36, 37] Previous structural alignment and targeted MD simulations with WT apo-HasAp, where the H32 loop was forced to move toward the closed loop conformation,[14] suggested that upon hemin loading hydrophobic contacts between Y138, M144, and hemin substituents elicit a tilting motion of α2, forcing an outward motion of the short loop comprised by G143 and D144 and perturbing interactions with the C-terminus of α1 leading to the H32 loop (Figure 8). Moreover, since in the absence of R33 the H32 loop moves spontaneously toward the Y75 loop, we speculate that the rearrangement of the C-terminus of α1 loosen interactions engaged by R33 and enable closure of the H32 loop.

The kinetic data show a perturbed transition from apo- to holo-HasAp in the R33A variant compared to the WT protein, suggesting that Tyr75 is not the first axial ligand to coordinate the heme iron. These data are consistent with an obstructed access to the hydrophobic platform on the Y75 loop by the closed configuration of the H32 loop in R33A apo-HasAp. The RFQ-RR data suggest that the initial coordination of the heme iron occurs with H32 (or other N-atom ligand) before the final coordination with H32 and Y75 is established. It is interesting to contrast this relatively slow loading of hemin in R33A apo-HasAp with the fast and apparently barrierless reaction of hemin with apo-$HasA_{yp}$.[16] Although both apo-proteins possess a pre-organized Y75 loop and closed H/Q32 loop, complete conversion to the holo form is at least 200 times slower in R33A-HasAp than in $HasA_{yp}$. Clearly, the Q32 loop in apo-$HasA_{yp}$ is evolutionary optimized to complement the hydrophobic platform on Y75 for the capture of hemin, while in R33A apo-HasAp, the nearly closed H32 loop must partly obstruct the hemin binding pocket. Future studies will aim to refine our putative model and define the essential networked residues that enable communication between the hemin binding site and the open H32 loop, so that hemin binding can trigger H32 loop closing.

Supplementary Material

Refer to Web version on PubMed Central for supplementary material.

Acknowledgments

Use of the University of Kansas Protein Structure Laboratory was supported by grants from the National Center for Research Resources (5P20RR017708) and the National Institute of General Medical Sciences (8P20GM103420) from the National Institutes of Health. Use of the IMCA-CAT beamline 17-ID at the Advanced Photon Source was supported by the companies of the Industrial Macromolecular Crystallography Association through a contract with Hauptman-Woodward Medical Research Institute. Use of the Advanced Photon Source was supported by the U.S.

Department of Energy, Office of Science, Office of Basic Energy Sciences, under Contract No. DE-AC02-06CH11357.

This study was supported by grants from the National Science Foundation, MCB1158469 to M.R., MCB0818488 to P.M.-L., MCB1157677 and XSEDE MCB070009 to W.I., and by a fellowship from the Japan Society for the Promotion of Science to H.M.

References

1. Nobles CL, Maresso AW. The theft of host heme by Gram-positive pathogenic bacteria. Metallomics : integrated biometal science. 2011; 3:788–796. [PubMed: 21725569]
2. Grigg JC, Ukpabi G, Gaudin CF, Murphy ME. Structural biology of heme binding in the Staphylococcus aureus Isd system. Journal of inorganic biochemistry. 2010; 104:341–348. [PubMed: 19853304]
3. Bullen JJ, Rogers HJ, Spalding PB, Ward CG. Iron and Infection: The Heart of the Matter. FEMS Immunol Med Microbiol. 2005; 43:325–330. [PubMed: 15708305]
4. Benson DR, Rivera M. Heme Uptake and Metabolism in Bacteria. Met Ions Life Sci. 2013:279–332. [PubMed: 23595676]
5. Andrews SC. Iron Storage in Bacteria. Advan Microbial Physiol. 1998; 40:281–351.
6. Reddy PV, Puri RV, Khera A, Tyagi AK. Iron storage proteins are essential for the survival and pathogenesis of Mycobacterium tuberculosis in THP-1 macrophages and the guinea pig model of infection. J Bacteriol. 2012; 194:567–575. [PubMed: 22101841]
7. Ghigo JM, Léttofé S, Wandersman C. A New Type of Hemophore-Dependent Heme Acquisition System of *Serratia Marcescens* Reconstituted in *Escherichia coli*. J Bacteriol. 1997; 179:3572–3579. [PubMed: 9171402]
8. Letoffe S, Ghigo JM, Wandersman C. Iron acquisition from heme and hemoglobin by a Serratia marcescens extracellular protein. Proceedings of the National Academy of Sciences of the United States of America. 1994; 91:9876–9880. [PubMed: 7937909]
9. Ghigo JM, Letoffe S, Wandersman C. A new type of hemophore-dependent heme acquisition system of Serratia marcescens reconstituted in Escherichia coli. Journal of bacteriology. 1997; 179:3572–3579. [PubMed: 9171402]
10. Marvig RL, Damkiaer S, Khademi SM, Markussen TM, Molin S, Jelsbak L. Within-host evolution of Pseudomonas aeruginosa reveals adaptation toward iron acquisition from hemoglobin. MBio. 2014; 5:e00966–00914. [PubMed: 24803516]
11. Smith AD, Wilks A. Differential contributions of the outer membrane receptors PhuR and HasR to heme acquisition in Pseudomonas aeruginosa. J Biol Chem. 2015; 290:7756–7766. [PubMed: 25616666]
12. Arnoux P, Haser R, Izadi N, Lecroisey A, Delepierre M, Wandersman C, Czjzek M. The crystal structure of HasA, a hemophore secreted by Serratia marcescens. Nature structural biology. 1999; 6:516–520. [PubMed: 10360351]
13. Wolff N, Izadi-Pruneyre N, Couprie J, Habeck M, Linge J, Rieping W, Wandersman C, Nilges M, Delepierre M, Lecroisey A. Comparative analysis of structural and dynamic properties of the loaded and unloaded hemophore HasA: functional implications. J Mol Biol. 2008; 376:517–525. [PubMed: 18164722]
14. Jepkorir G, Rodriguez JC, Rui H, Im W, Lovell S, Battaile KP, Alontaga AY, Yukl ET, Moenne-Loccoz P, Rivera M. Structural, NMR spectroscopic, and computational investigation of hemin loading in the hemophore HasAp from Pseudomonas aeruginosa. Journal of the American Chemical Society. 2010; 132:9857–9872. [PubMed: 20572666]
15. Alontaga AY, Rodriguez JC, Schonbrunn E, Becker A, Funke T, Yukl ET, Hayashi T, Stobaugh J, Moenne-Loccoz P, Rivera M. Structural characterization of the hemophore HasAp from Pseudomonas aeruginosa: NMR spectroscopy reveals protein-protein interactions between Holo-HasAp and hemoglobin. Biochemistry. 2009; 48:96–109. [PubMed: 19072037]
16. Kumar R, Lovell S, Matsumura H, Battaile KP, Moenne-Loccoz P, Rivera M. The hemophore HasA from Yersinia pestis (HasAyp) coordinates hemin with a single residue, Tyr75, and with minimal conformational change. Biochemistry. 2013; 52:2705–2707. [PubMed: 23578210]

17. Yukl ET, Jepkorir G, Alontaga AY, Pautsch L, Rodriguez JC, Rivera M, Moenne-Loccoz P. Kinetic and spectroscopic studies of hemin acquisition in the hemophore HasAp from Pseudomonas aeruginosa. Biochemistry. 2010; 49:6646–6654. [PubMed: 20586423]
18. Kabsch W. Xds, *Acta crystallographica*. Section D, Biological crystallography. 2010; 66:125–132.
19. Ahn HC, Le YTH, Nagchowdhuri PS, Derose EF, Putnam-Evans C, London RE, Markley JL. NMR Characterization of an Amyloidogenic Conformational Ensemble of the PI3K SH3 Domain. Protein Sci. 2006; 15:2552–2557. [PubMed: 17001038]
20. Kabsch W. Automatic-Indexing of Rotation Diffraction Patterns. J Appl Crystallogr. 1988; 21:67–71.
21. McCoy AJ, Grosse-Kunstleve RW, Adams PD, Winn MD, Storoni LC, Read RJ. *Phaser* crystallographic software. J Appl Cryst. 2007; 40:658–674. [PubMed: 19461840]
22. Adams PD, Afonine PV, Bunkoczi G, Chen VB, Davis IW, Echols N, Headd JJ, Hung LW, Kapral GJ, Grosse-Kunstleve RW, McCoy AJ, Moriarty NW, Oeffner R, Read RJ, Richardson DC, Richardson JS, Terwilliger TC, Zwart PH. PHENIX: a comprehensive Python-based system for macromolecular structure solution, *Acta crystallographica*. Section D, Biological crystallography. 2010; 66:213–221.
23. Emsley P, Cowtan K. Coot: model-building tools for molecular graphics, *Acta crystallographica*. Section D, Biological crystallography. 2004; 60:2126–2132.
24. Lovell SC, Davis IW, Arendall WB 3rd, de Bakker PI, Word JM, Prisant MG, Richardson JS, Richardson DC. Structure validation by Calpha geometry: phi, psi and Cbeta deviation. Proteins. 2003; 50:437–450. [PubMed: 12557186]
25. Potterton L, McNicholas S, Krissinel E, Gruber J, Cowtan K, Emsley P, Murshudov GN, Cohen S, Perrakis A, Noble M. Developments in the CCP4 molecular-graphics project. Acta Crystallogr D Biol Crystallogr. 2004; 60:2288–2294. [PubMed: 15572783]
26. Schrodinger LLC. The PyMOL Molecular Graphics System, Version 1.3r1. 2010
27. Kantardjieff KA, Rupp B. Matthews coefficient probabilities: Improved estimates for unit cell contents of proteins, DNA, and protein-nucleic acid complex crystals. Protein Sci. 2003; 12:1865–1871. [PubMed: 12930986]
28. Matthews BW. Solvent Content of Protein Crystals. J Mol Biol. 1968; 33:491–497. [PubMed: 5700707]
29. Jo S, Kim T, Iyer VG, Im W. CHARMM-GUI: a web-based graphical user interface for CHARMM. Journal of computational chemistry. 2008; 29:1859–1865. [PubMed: 18351591]
30. Lee J, Cheng X, Swails JM, Yeom MS, Eastman PK, Lemkul JA, Wei S, Buckner J, Jeong JC, Qi Y, Jo S, Pande VS, Case DA, Brooks CL 3rd, MacKerell AD Jr, Klauda JB, Im W. CHARMM-GUI Input Generator for NAMD, GROMACS, AMBER, OpenMM, and CHARMM/OpenMM Simulations Using the CHARMM36 Additive Force Field. Journal of chemical theory and computation. 2016; 12:405–413. [PubMed: 26631602]
31. Brooks BR, Brooks CL III, Mackerell AD Jr, Nilsson L, Petrella RJ, Roux B, Won Y, Archontis G, Bartels C, Boresch S, Caflisch A, Caves L, Cui Q, Dinner AR, Feig M, Fischer S, Gao J, Hodoscek M, Im W, Kuczera K, Lazaridis T, Ma J, Ovchinnikov V, Paci E, Pastor RW, Post CB, Pu JZ, Schaefer M, Tidor B, Venable RM, Woodcock HL, Wu X, Yang W, York DM, Karplus M. CHARMM: The Biomolecular Simulation Program. J Comput Chem. 2009; 30:1545–1614. [PubMed: 19444816]
32. Jo S, Cheng X, Islam SM, Huang L, Rui H, Zhu A, Lee HS, Qi Y, Han W, Vanommeslaeghe K, MacKerell AD Jr, Roux B, Im W. CHARMM-GUI PDB manipulator for advanced modeling and simulations of proteins containing nonstandard residues. Advances in protein chemistry and structural biology. 2014; 96:235–265. [PubMed: 25443960]
33. Huang J, MacKerell AD Jr. CHARMM36 all-atom additive protein force field: validation based on comparison to NMR data. Journal of computational chemistry. 2013; 34:2135–2145. [PubMed: 23832629]
34. Phillips JC, Braun R, Wang W, Gumbart J, Tajkhorshid E, Villa E, Chipot C, Skeel RD, Kale L, Schulten K. Scalable molecular dynamics with NAMD. Journal of computational chemistry. 2005; 26:1781–1802. [PubMed: 16222654]

35. Feller SE, Zhang Y, Pastor RW. Constant Pressure Molecular Dynamics Simulation: The Langevin Piston Method. J Chem Phys. 1995; 103:4613–4621.
36. Martyna GJ, Tobias DJ, Klein ML. Constant pressure molecular dynamics algorithms. J Chem Phys. 1994; 101:4177.
37. Steinbach PJ, Brooks BR. New Spherical-Cutoff Methods for Long-Range Forces in Macromolecular Simulation. Journal of computational chemistry. 1994; 15:667–683.
38. Essmann U, Perera L, Berkowitz ML, Darden T, Lee H, Pedersen LG. A smooth particle mesh Ewald method. J Chem Phys. 1995; 103:8577.
39. Matsumura H, Moenne-Loccoz P. Characterizing millisecond intermediates in hemoproteins using rapid-freeze-quench resonance Raman spectroscopy. Methods Mol Biol. 2014; 1122:107–123. [PubMed: 24639256]
40. Kumar R, Matsumura H, Lovell S, Yao H, Rodriguez JC, Battaile KP, Moenne-Loccoz P, Rivera M. Replacing the Axial Ligand Tyrosine 75 or Its Hydrogen Bond Partner Histidine 83 Minimally Affects Hemin Acquisition by the Hemophore HasAp from Pseudomonas aeruginosa. Biochemistry. 2014; 53:2112–2125. [PubMed: 24625274]
41. Krissinel E, Henrick K. Secondary-structure matching (SSM), a new tool for fast protein structure alignment in three dimensions, *Acta crystallographica*. Section D, Biological crystallography. 2004; 60:2256–2268.
42. Evans PR. An introduction to data reduction: space-group determination, scaling and intensity statistics. Acta Crystallogr D Biol Crystallogr. 2011; 67:282–292. [PubMed: 21460446]
43. Evans P. Scaling and assessment of data quality. Acta Crystallogr D Biol Crystallogr. 2006; 62:72–82. [PubMed: 16369096]
44. Diederichs K, Karplus PA. Improved R-factors for diffraction data analysis in macromolecular crystallography. Nat Struct Biol. 1997; 4:269–275. [PubMed: 9095194]
45. Weiss MS. Global indicators of X-ray data quality. Journal of Applied Crystallography. 2001; 34:130–135.
46. Karplus PA, Diederichs K. Linking crystallographic model and data quality. Science. 2012; 336:1030–1033. [PubMed: 22628654]
47. Evans P. Biochemistry. Resolving some old problems in protein crystallography. Science. 2012; 336:986–987. [PubMed: 22628641]

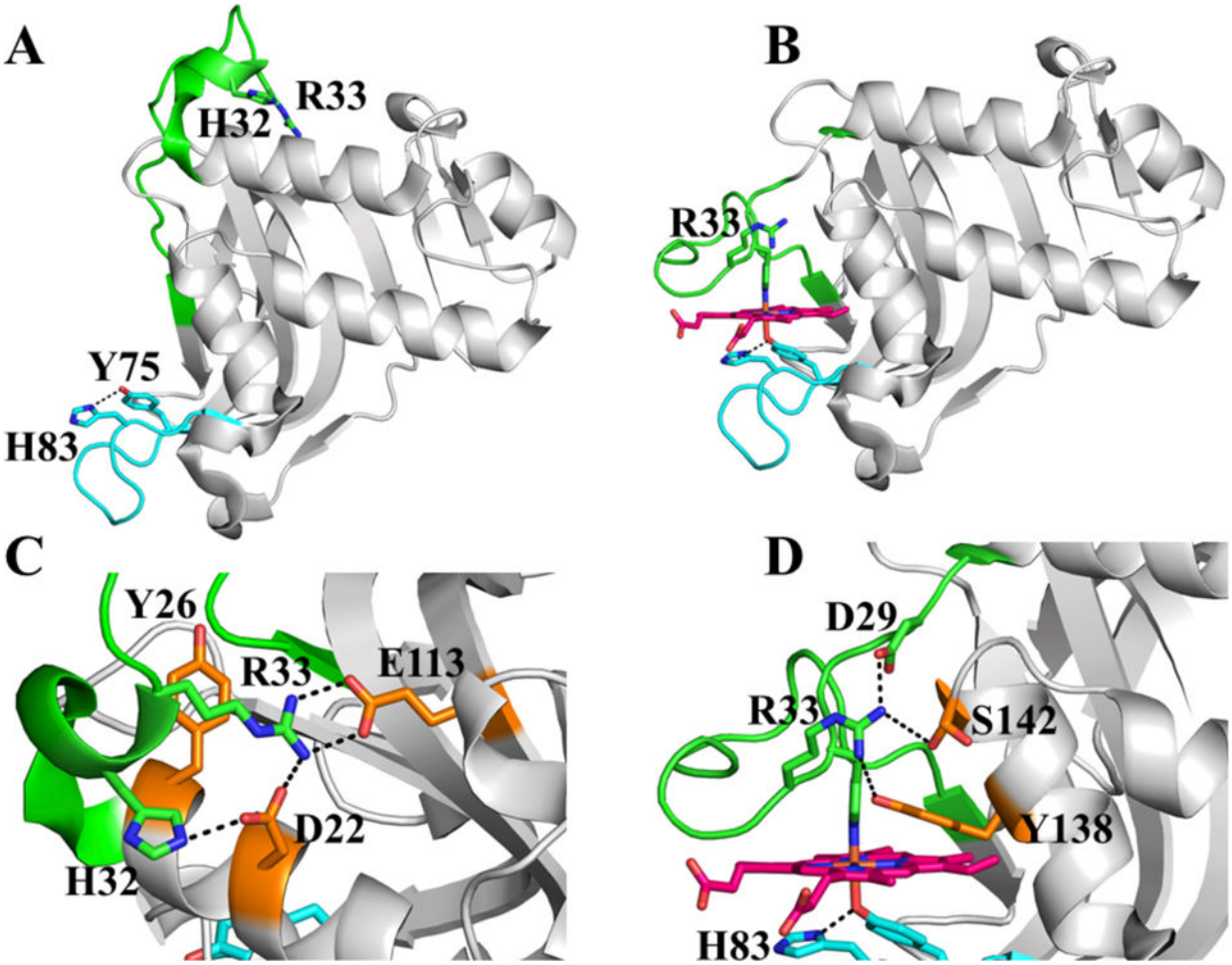

Figure 1.

Crystal structure of (A) apo-HasAp (PDB code: 3MOK) and (B) apo-HasAp (PDB code: 3ELL) showing the Y75 loop (green) and H32 loop (magenta) and the R33 location in the structures. Heme is shown in crimson red. Heme loads onto the Y75 loop, which triggers the closure of the H32 loop, thus coordinating the heme iron by His32. Zoomed-in views of interactions contributing to stabilizing the H32 loop in apo- and holo-HasAp are shown in (C) and (D), respectively.

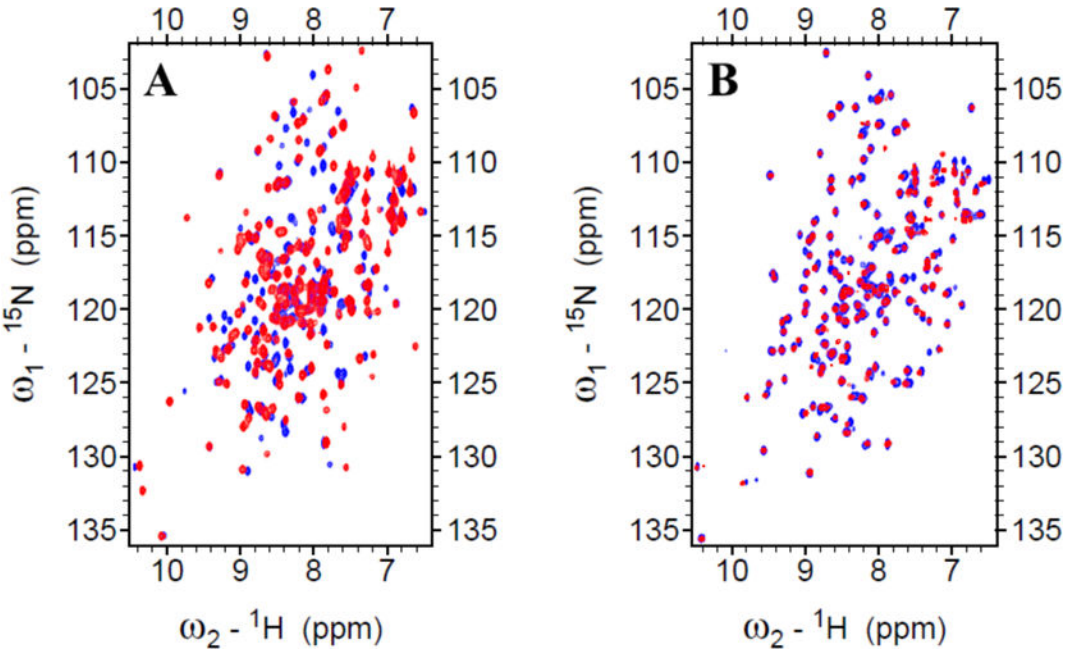

Figure 2.

Superimposed ^{1}H, ^{15}N-HSQC spectra of: (A) WT apo-HasAp (red) and R33A apo-HasAp (blue), and (B) WT holo-HasAp (red) and R33A holo-HasAp. Spectra were obtained at 32 °C as described in the Experimental Procedures.

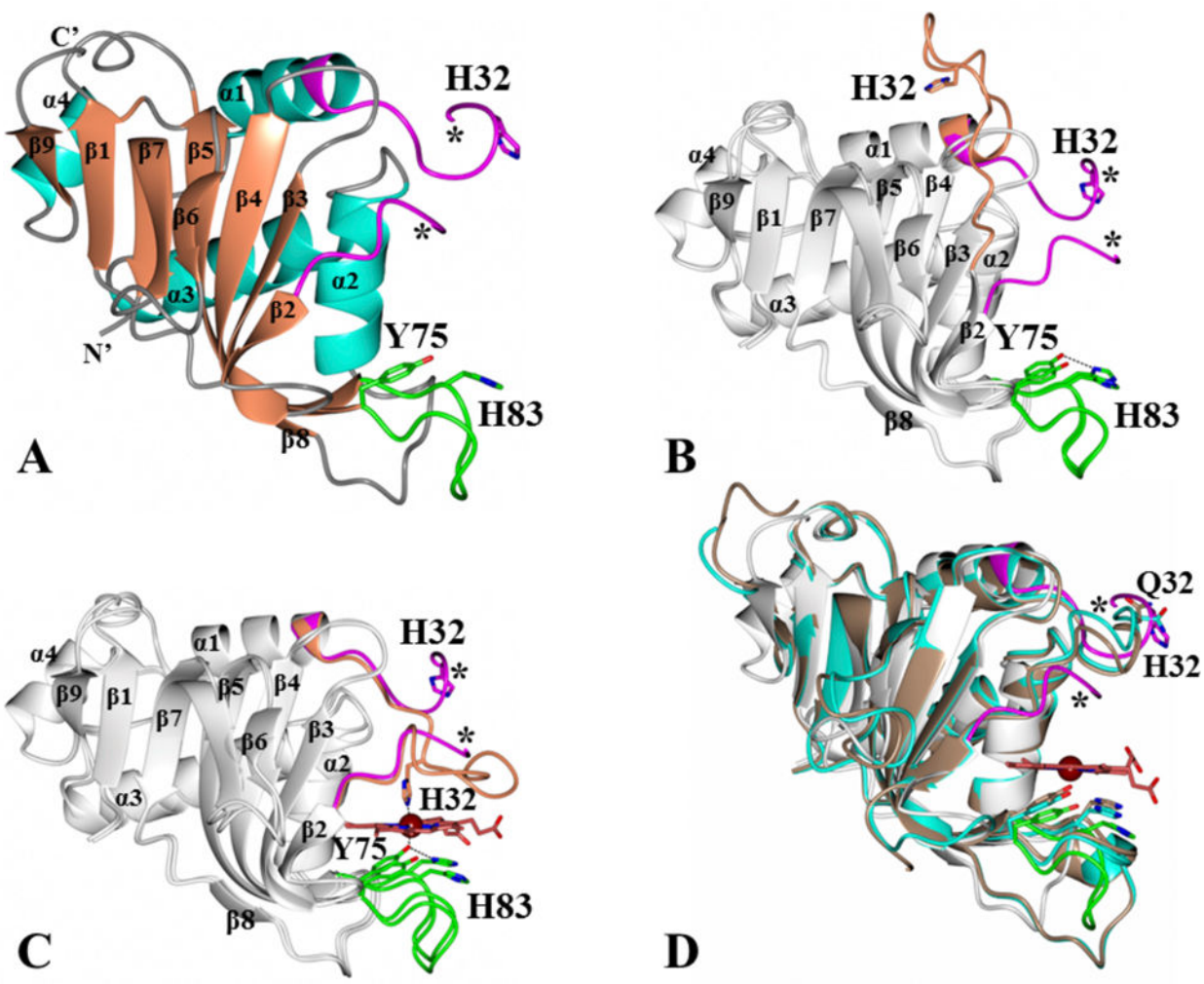

Figure 3.

(A) Crystal structure of R33A apo-HasAp. The H32 and Y75 loops are shown in magenta and green respectively. Asterisks denote missing electron density between Gly35 and Asp39. (B–D) Structural superposition of R33A apo-HasAp with: (B) WT apo-HasAp (PDB code: 3MOK), (C) WT holo-HasAp (PDB code: 3ELL) and (D) WT apo-$HasA_{yp}$ (brown, PDB code: 4JER), and WT holo-$HasA_{yp}$ (cyan, PDB code: 4JET). Heme in the holo-structures is shown as orange sticks with the heme-iron rendered as a sphere.

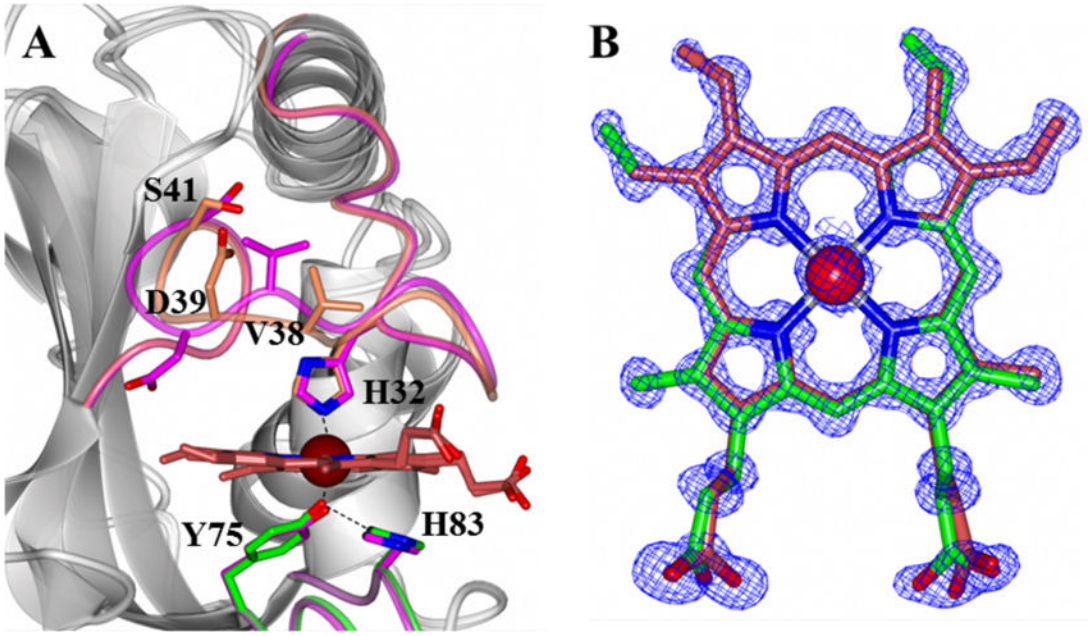

Figure 4.

(A) Superimposed structures of WT holo-HasAp (PDB code: 3ELL) and R33A holo-HasAp. The H32 loop in the WT protein is shown in orange, while that of the R33 mutant is in magenta. (B) F_o-F_c electron density omit map contoured at 3σ showing the two orientation of the hemin molecule (crimson red and green) bound to R33A holo-HasAp.

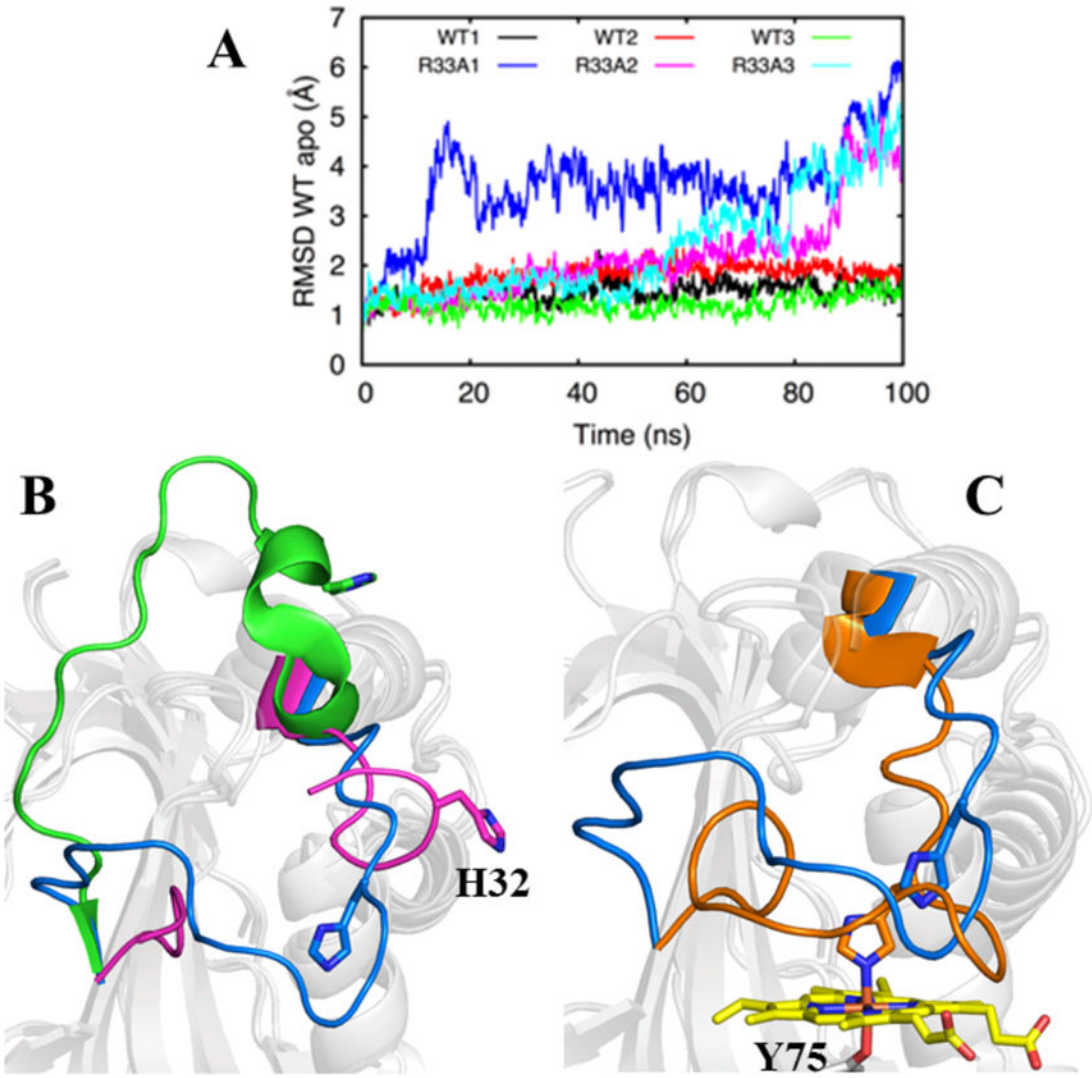

Figure 5.

(A) RMSD plot showing the time-dependent RMSD observed during 100 ns trajectories for WT apo- and R33A apo-HasAp. Systems A1, A2 and A3 are color coded as indicated in the plot. (B) Structural superposition of the model obtained at the end of the MD trajectory obtained from system R33A1 (blue) and the X-ray crystal structures of WT apo-HasAp (green, PDB code: 3MOK) and R33A apo-HasAp (magenta). (C) Structural superposition of the model obtained at the end of the MD trajectory obtained from system R33A1 (blue) and the X-ray crystal structure of WT holo-HasAp (orange; PDB code: 3ELL).

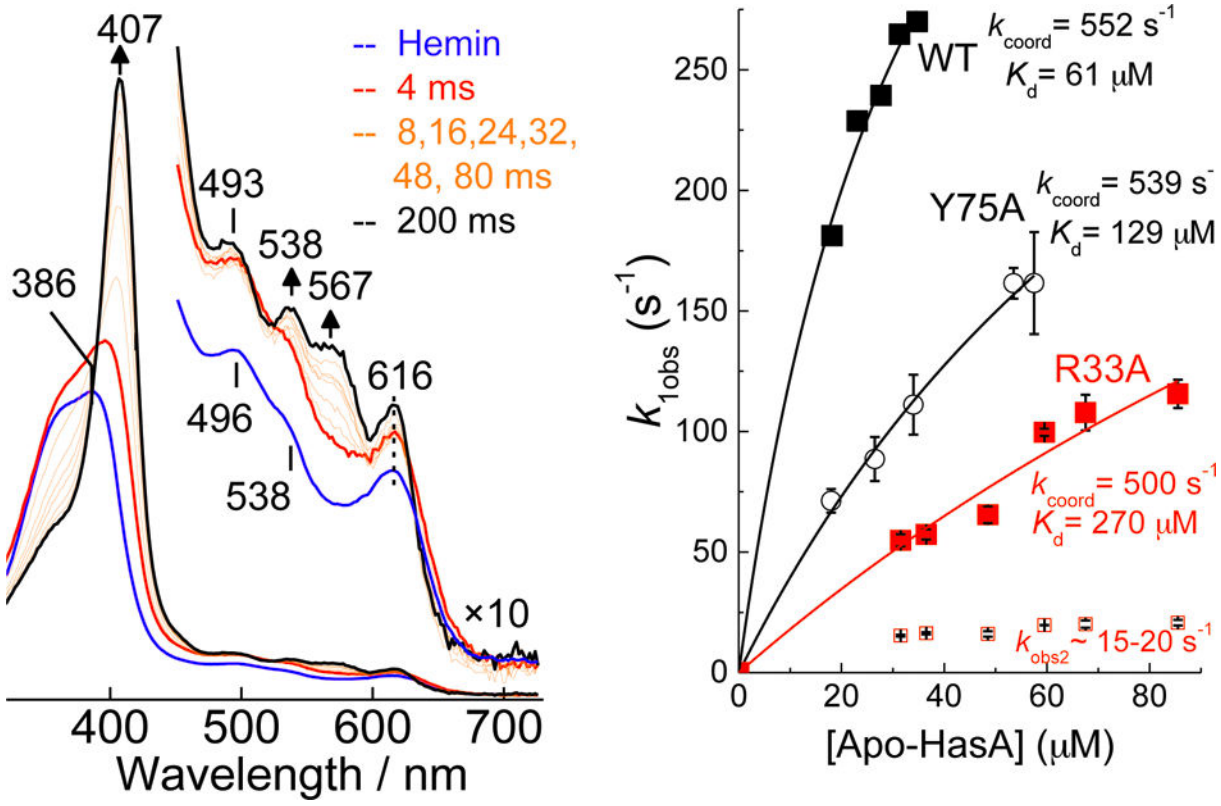

Figure 6.

Stopped-flow absorption spectra of the association of hemin with 60 μM R33A apo-HasAp at 4 °C. The blue trace is a hemin/buffer control. Also shown are plots of the observed rates vs apo-HasAp concentrations for the R33A variant and previously determined k_{obs1} for the WT protein and Y75A variant.

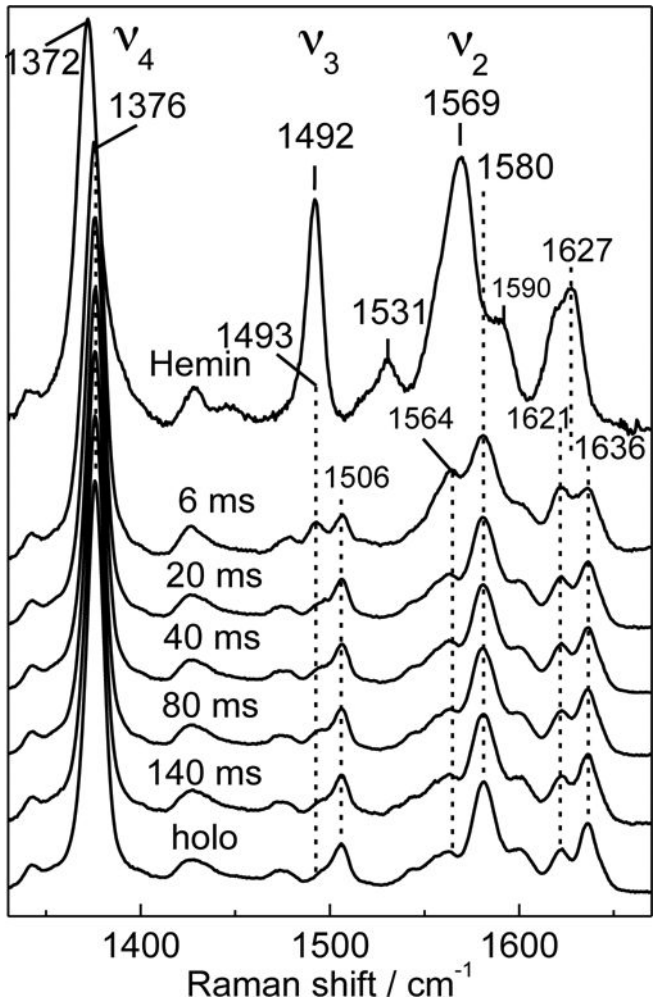

Figure 7.

High-frequency RR spectra of the RFQ samples of the reaction of 1 equiv of hemin with R33A apo-HasAp (protein concentration after mixing 300 μM; 406-nm excitation wavelength; all spectra are normalized on the porphyrin ν_4 mode; the top trace corresponds to the spectrum of free hemin obtained in the same conditions).

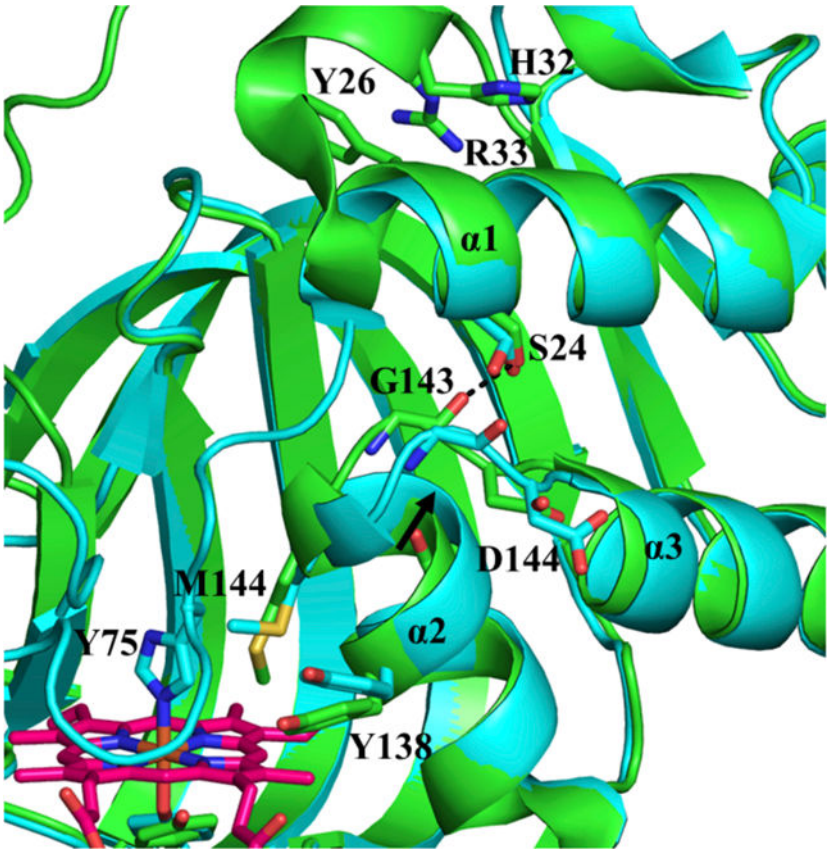

Figure 8.

Putative model of the mechanism whereby hemin binding at the Y75 loop in HasAp triggers closing of the H32 loop. Superposition of WT apo-HasAp (green,) and holo-HasAp (cyan) structures shows an outward tilting of the α2 helix to relieve steric hindrance between the side chains of Y138 and M144 and incoming hemin. The outward motion of α2 severs a H-bond between G143 and S24, which is located in α1, immediately before the kink leading to the H32 loop and possibly induces conformational disorder in the C-terminus of α1, loosening R33 interactions and enabling the H32 loop to close.

Scheme 1.

Two-step model for the first coordination step of hemin to apo HasAp

Table 1

X-ray diffraction and refinement statistics for R33A HasAp

	R33A apo-HasAp	R33A holo-HasAp
Data Collection		
Unit-cell parameters (Å, °)	$a=b$=92.78, c=95.71	a= 34.17, b= 47.17, c=101.37
Space group	$P4_12_12$	$P2_12_12_1$
Resolution (Å)[1]	47.86–1.95 (2.00–1.95)	47.16–1.05 (1.07–1.05)
Wavelength (Å)	1.0000	1.0000
Temperature (K)	100	100
Observed reflections	402,726	484,999
Unique reflections	31,128	75,527
$<I/\sigma(I)>$[1]	21.2 (2.1)	15.3 (3.3)
Completeness (%)[1]	100 (100)	97.8 (94.4)
Multiplicity[1]	12.9 (13.2)	6.4 (6.2)
R_{merge} (%)[1, 2]	7.9 (177.1)	6.5 (56.1)
R_{meas} (%)[1, 4]	8.3 (184.2)	7.1 (61.2)
R_{pim} (%)[1, 4]	2.3 (50.2)	2.8 (24.1)
$CC_{1/2}$[1, 5]	1.000 (0.894)	0.999 (0.859)
Refinement		
Resolution (Å)	33.31–1.95	34.53–1.05
Reflections[6] (working/test)	55,227 / 2,852	71,679 / 3,772
R_{factor} / R_{free} (%)[3]	18.5 / 21.2	11.3 / 12.9
No. of atoms (Protein/Heme/Water)	1,290 / 0 / 72	1,413 / 86 / 230
Model Quality		
R.m.s deviations		
Bond lengths (Å)	0.010	0.008
Bond angles (°)	1.140	1.052
Average B-factor (Å^2)		
All Atoms	47.8	11.6
Protein	47.4	9.6
Heme	–	7.9
Water	52.0	24.1
Coordinate error, maximum likelihood (Å)	0.20	0.05
Ramachandran Plot		
Most favored (%)	93.8	98.0
Additionally allowed (%)	6.2	2.0

[1)] Values in parenthesis are for the highest resolution shell.

[2] $R_{merge} = S_{hkl} S_i |I_i(hkl) - \langle I(hkl) \rangle| / S_{hkl} S_i I_i(hkl)$, where $I_i(hkl)$ is the intensity measured for the ith reflection and $\langle I(hkl) \rangle$ is the average intensity of all reflections with indices hkl.

[3] $R_{factor} = S_{hkl} \| F_{obs}(hkl) | - |F_{calc}(hkl) \| / S_{hkl} |F_{obs}(hkl)|$; Rfree is calculated in an identical manner using 5% of randomly selected reflections that were not included in the refinement.

[4] R_{meas} = redundancy-independent (multiplicity-weighted) R_{merge}[42,43]. R_{pim} = precision-indicating (multiplicity-weighted) R_{merge}[44,45].

[5] $CC_{1/2}$ is the correlation coefficient of the mean intensities between two random half-sets of data[46,47].

[6] For R33A apo-HasAp, the number of reflections used during refinement is greater than the number unique reflections reported for data scaling. This is due to the fact that Friedel pairs were kept separate during refinement and the anomalous scattering factors for the Cd^{2+} atoms were refined.

Table 2

List of interaction in the H32 loop with the body of the protein

H32 loop residues	Distance (Å)	Interacting residues
Asp29 (N)	3.2	Tyr26 (O)
His32 (Nε)	2.8	Asp22 (Oδ)
Arg33 (NH)	2.8	Glu113(Oε)
Arg33 (NH)	3.0	Asp22 (Oδ)
Val37(O)	3.1	Asp64 (Oδ)
Asp39 (N)	2.9	Asp64 (Oδ)
Gly40 (N)	2.9	Asp64 (Oδ)
Asn42 (Nδ)	2.8	Gly100 (O)
Thr43 (O)	3.2	Lys59 (N)
Gly45 (N)	2.8	Ala57 (O)